



## **BROADBAND TIME HISTORY SIMULATION USING A HYBRID APPROACH**

**Robert GRAVES<sup>1</sup> and Arben PITARKA<sup>2</sup>**

### **SUMMARY**

We present a methodology for generating broadband (0 - 10 Hz) ground motion time histories for moderate and larger crustal earthquakes. Our hybrid technique combines a stochastic approach at high frequencies with a deterministic approach at low frequencies. The broadband response is obtained by summing the separate responses in the time domain using matched filters centered at 1 Hz. We use a kinematic description of fault rupture, incorporating spatial heterogeneity in slip, rupture velocity and rise time by discretizing an extended finite-fault into a number of smaller subfaults. The stochastic approach sums the response for each subfault assuming a random phase, an omega-squared source spectrum and generic ray-path Green's functions. Gross impedance effects are incorporated using quarter wavelength theory to bring the response to a reference baserock velocity level. The deterministic approach sums the response for many point sources distributed across each subfault. Wave propagation at frequencies below 1 Hz is modeled using a 3D viscoelastic finite difference algorithm with the minimum shear wave velocity set between 600 and 1000 m/s, depending on the scope and complexity of the velocity structure. To account for site-specific geologic conditions, short- and mid-period empirical amplification factors provided by Borchardt [1] are used to develop frequency-dependent non-linear site response functions. The amplification functions are applied to the stochastic and deterministic responses separately since these may have different (computational) reference site velocities. We note that although the amplification factors are strictly defined for response spectra, we have applied them to the Fourier amplitude spectra of our simulated time histories. This process appears to be justified because the amplification functions vary slowly with frequency and the method produces favorable comparisons with observations. We demonstrate the applicability of the technique by modeling the broadband strong ground motion recordings from the 1989 Loma Prieta and 1994 Northridge earthquakes.

### **INTRODUCTION**

Our primary motivation in developing an enhanced broadband simulation methodology is to provide more robust estimates of the ground shaking expected in future earthquakes. The most comprehensive manner of ground shaking characterization is through the use of full waveform time histories. These ground motion time histories can have many potential applications, including engineering design studies

---

<sup>1</sup> Principal Scientist, URS Corporation, Pasadena, CA, USA. Email: robert\_graves@urscorp.com

<sup>2</sup> Senior Project Scientist, URS Corporation, Pasadena, CA, USA. Email: arben\_pitarka@urscorp.com

incorporating non-linear structural analysis, seismic hazard characterization, disaster mitigation planning and high-resolution real time and post earthquake (e.g., ShakeMap) ground motion estimation. Traditionally, ground motion recordings from past earthquakes have been used as surrogates to represent the motions expected during future earthquakes. Unfortunately, the library of existing recordings only samples a small subset of possible earthquake scenarios. Thus, the ground motion records typically must be scaled or modified in order to fit the magnitude, mechanism, distance and site characteristics of the target earthquake. As an alternative, advances in the understanding of fault rupture processes, wave propagation phenomena and site response characterization, coupled with the tremendous growth in computational power and efficiency, has made the prospect of large-scale ground motion time history synthesis for future earthquakes much more feasible.

The idea of simulating broadband strong ground motion time histories is not new, and dates back at least to the pioneering work of Hartzell [2] and Irikura [3]. These early studies proposed a method of summing recordings of small earthquakes (empirical Green's functions) to estimate the response of a larger earthquake. Since then, the simulation techniques have been extended to include stochastic representation of source and path effects (e.g., Boore [4]), theoretical full waveform Green's functions (e.g., Zeng, [5]), or various combinations of these approaches (e.g., Hartzell [6]). Over the years, a large number of investigators have made significant contributions and refinements to these methodologies. Hartzell [7] provides a detailed and comprehensive review of many of these existing simulation methodologies.

In our approach, the broadband ground motion simulation procedure is a hybrid technique that computes the low frequency and high frequency ranges separately and then combines the two to produce a single time history (Hartzell [7]). At frequencies below 1 Hz, the methodology is deterministic and contains a theoretically rigorous representation of fault rupture and wave propagation effects, and attempts to reproduce recorded ground motion waveforms and amplitudes. At frequencies above 1 Hz, it uses a stochastic representation of source radiation, which is combined with a simplified theoretical representation of wave propagation and scattering effects. The use of different simulation approaches for the different frequency bands results from the seismological observation that source radiation and wave propagation effects tend to become stochastic at frequencies of about 1 Hz and higher.

Our methodology offers a significant enhancement over previous broadband simulation techniques through the use of frequency-dependent non-linear site amplification factors. These factors are incorporated by first restricting the computational velocity model in both the deterministic and stochastic bandwidths to have an average near-surface shear wave velocity between 600 and 1000 m/s. We then apply site-specific amplification factors, which are derived using the empirical relations of Borchardt [1]. This approach significantly reduces the numerical computational burden, particularly for the deterministic domain, and also provides an efficient mechanism for including detailed site-specific geologic information in the ground motion estimates.

In the sections that follow, we first provide detailed descriptions of the deterministic and stochastic simulation methodologies. Next, we discuss the derivation and implementation of the non-linear site amplification factors. The final sections present validation studies of the simulation methodology using ground motions recorded during the 1989 Loma Prieta and 1994 Northridge earthquakes.

## **SIMULATION METHODOLOGY**

### **Deterministic Methodology ( $f < 1$ Hz)**

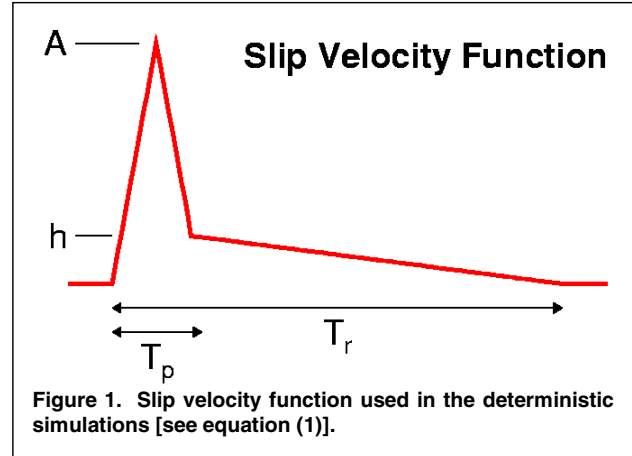
The low frequency simulation methodology uses a deterministic representation of source and wave propagation effects and is based on the approach described by Hartzell [8]. The basic calculation is carried out using a 3D viscoelastic finite-difference algorithm, which incorporates both complex source

rupture as well as wave propagation effects within arbitrarily heterogeneous 3D geologic structure. The details of the finite-difference methodology are described by Graves [9] and Pitarka [10]. Anelasticity is incorporated using the coarse-grain approach of Day [11].

The earthquake source is specified by a kinematic description of fault rupture, incorporating spatial heterogeneity in slip, rupture velocity and rise time. Following Hartzell [8], the fault is divided into a number of subfaults. The slip and rise time are constant across each individual subfault, although these parameters are allowed to vary from subfault to subfault. We use a slip velocity function that is constructed using two triangles as shown in Figure 1. This functional form is based on results of dynamic rupture simulations (e.g., Guatteri [12]). We constrain the parameters of this function as follows:

$$\begin{aligned} T_r &= 1.83 \times 10^{-9} \cdot M_0^{-1/3} \\ T_p &= 0.2 \cdot T_r \\ h &= 0.2 \cdot A \end{aligned} \quad (1)$$

where  $M_0$  is the seismic moment,  $T_r$  is the rise time and  $A$  is normalized to give the desired final slip. The expression for  $T_r$  comes from the empirical analysis of Somerville [13]. In general,  $T_r$  may vary across the fault; however, in practice we only allow a depth dependent scaling such that  $T_r$  increases by a factor of 2 if the rupture is between 0 and 5 km depth. This is consistent with observations of low slip velocity on shallow fault ruptures (Kagawa [14]).



The rupture initiation time ( $T_i$ ) is determined using the expression

$$\begin{aligned} T_i &= R/V_r - \delta t \\ V_r &= 0.8 \cdot V_s \end{aligned} \quad (2)$$

where  $R$  is the rupture path length from the hypocenter to a given point on the fault surface,  $V_r$  is the rupture velocity and is set at 80% of the local shear wave velocity ( $V_s$ ), and  $\delta t$  is a timing perturbation that scales linearly with slip amplitude such that  $\delta t = \delta t_0$  where the slip is at its maximum and  $\delta t = 0$  where the slip is at the average slip value. We typically set  $\delta t_0 = 0.5$  sec. This scaling results in faster rupture across portions of the fault having large slip as suggested by source inversions of past earthquakes (Hisada [15]).

For scenario earthquakes, the slip distribution can be specified using randomized spatial fields, constrained to fit certain wave number properties (e.g., Somerville [13]; Mai [16]). In the simulation of past earthquakes, we use smooth representations of the static slip distribution determined from finite-fault source inversions. Typically, these inversions will also include detailed information on the spatial variation of rupture initiation time and slip velocity function, either by solving for these parameters directly or by using multiple time windows. However, we do not include these in our simulations, but rather rely on equations (1) and (2) to provide them. Our philosophy is that the level of detailed resolution of these parameters provided by the source inversions will generally not be available *a priori* for future earthquakes. Furthermore, since the inversions determine these parameters by optimally fitting the

selected observations, there are no guarantees that they will produce an optimal waveform fit at sites not used in the inversion. Hopefully, an improved understanding of dynamic rupture processes will help to provide better constraints on these parameters in the future.

### Stochastic Methodology ( $f > 1$ Hz)

The high frequency simulation methodology is a stochastic approach that sums the response for each subfault assuming a random phase, an omega-squared source spectrum and simplified Green's functions. The methodology follows from the procedure that was first presented by Boore [4] with the extension to finite-faults given by Beresnev [17]. We have incorporated several modifications of the original finite-fault methodology of Beresnev [17], which are described below.

In our approach, each subfault is allowed to rupture with a subfault moment weighting that is proportional to the final static slip amount given by the prescribed rupture model. The final summed moment release is then scaled to the prescribed target mainshock moment. This alleviates the problem of requiring that each of the subfaults scale to an integer multiple of  $\sigma_p \cdot dl^3$  (where  $\sigma_p$  is the stress parameter and  $dl$  is the subfault dimension), which tends to make many of the subfaults have zero moment release. The subfault dimensions are determined using the scaling relation of Beresnev [18].

Beresnev [19] define a radiation-strength factor ( $s$ ), which is used as a free parameter in the specification of the subfault corner frequency ( $f_c$ )

$$f_c = s \cdot z \frac{V_r}{\pi \cdot dl} \quad (3)$$

where  $z$  is a scaling factor relating  $f_c$  to the rise time of the subfault source. In our approach, instead of allowing this to be a free parameter, we set  $z = 1.6$  and let

$$s = D_f \cdot A_f \quad (4)$$

$$D_f = \begin{cases} 1 & \text{if } h < h_0 \\ 1 + c_0 \frac{h - h_0}{h_1 - h_0} & \text{if } h_0 \leq h \leq h_1 \\ 1 + c_0 & \text{if } h \geq h_1 \end{cases}$$

$$A_f = \begin{cases} 1 & \text{if } \delta > \delta_1 \\ 1 + c_1 \frac{\delta_1 - \delta}{\delta_1 - \delta_0} & \text{if } \delta_1 \geq \delta \geq \delta_0 \\ 1 + c_1 & \text{if } \delta < \delta_0 \end{cases}$$

where  $D_f$  is a depth scaling factor,  $h_0 = 5$  km,  $h_1 = 10$  km and  $h$  is the depth of the subfault center in km, and  $A_f$  is a dip scaling factor,  $\delta_0 = 45^\circ$ ,  $\delta_1 = 60^\circ$  and  $\delta$  is the subfault dip. The constants  $c_0$  and  $c_1$  are set at 0.4 and 0.35, respectively, based on calibration experiments. This parameterization follows from the observation in crustal earthquakes that slip velocity is relatively low for shallow near-vertical ruptures and increases with increasing rupture depth and decreasing fault dip (Kagawa [14]). Since corner frequency is proportional to slip velocity, this formulation replicates the trend of the observations. We note that although this formulation reduces the number of free parameters, it certainly is not unique and probably has trade-offs with other parameters in the stochastic model. In particular, allowing the subfault stress parameter ( $\sigma_p$ ) to be variable across the fault would accommodate a similar type of slip velocity scaling. Instead, we fix  $\sigma_p = 50$  in our simulations.

Our formulation also allows the specification of a plane layered velocity model from which we calculate simplified Green's functions (GFs) and impedance effects. The GFs are comprised of the direct and Moho-reflected rays, which are traced through the specified velocity structure. Following Ou [20], each ray is attenuated by  $1/R_p$  where  $R_p$  is the path length traveled by the particular ray. For each ray and each subfault, we calculate a radiation pattern coefficient by averaging over a range of slip mechanisms and take-off angles, varying  $\pm 45^\circ$  about their theoretical values. Anelasticity is incorporated using a travel-time weighted average of the  $Q$  values for each of the velocity layers and using a kappa operator set at  $\kappa = 0.05$ . Finally, gross impedance effects are included using quarter wavelength theory (Boore [21]) to derive amplification functions that are consistent with the specified velocity structure.

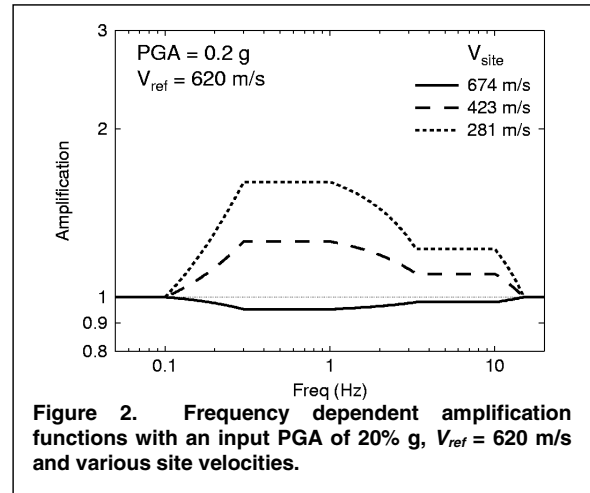
### Site Specific Amplification Factors

Borcherdt [1] derived empirically based amplification functions for use in converting response spectra from one site condition to a different site condition. The general form of these functions is given by

$$F_x = (V_{site} / V_{ref})^{m_x} \quad (5)$$

where  $V_{site}$  is the 30 m travel-time averaged shear wave velocity ( $V_s^{30}$ ) at the site of interest,  $V_{ref}$  is the corresponding velocity measure at a reference site where the ground response is known, and  $m_x$  is an empirically determined factor. Borcherdt [1] specified one set of factors at short periods (centered around 0.3 s) and one set at mid-periods (centered around 1.0 s). Furthermore, non-linear effects are included since the  $m_x$  decrease as the reference ground response PGA increases. The decrease in the  $m_x$  is sharper for the short period factors than the mid-period ones, reflecting the observed increase of non-linear effects at shorter periods.

In our simulation methodology, we restrict the computational velocity models in both the deterministic and stochastic calculations to have  $V_s^{30}$  values between 600 and 1000 m/s. This is our  $V_{ref}$ . To obtain an amplification function for a given site velocity, we first determine the short- and mid-period factors from equation (5) using the tabulated  $m_x$  from Borcherdt [1] given the reference PGA from the stochastic response. Next, we construct a smoothly varying function in the frequency domain by applying a simple taper to interpolate the factors between the short- and mid-period bands. The function tapers back to unity at very short and very long periods. An example set of these functions is shown in Figure 2



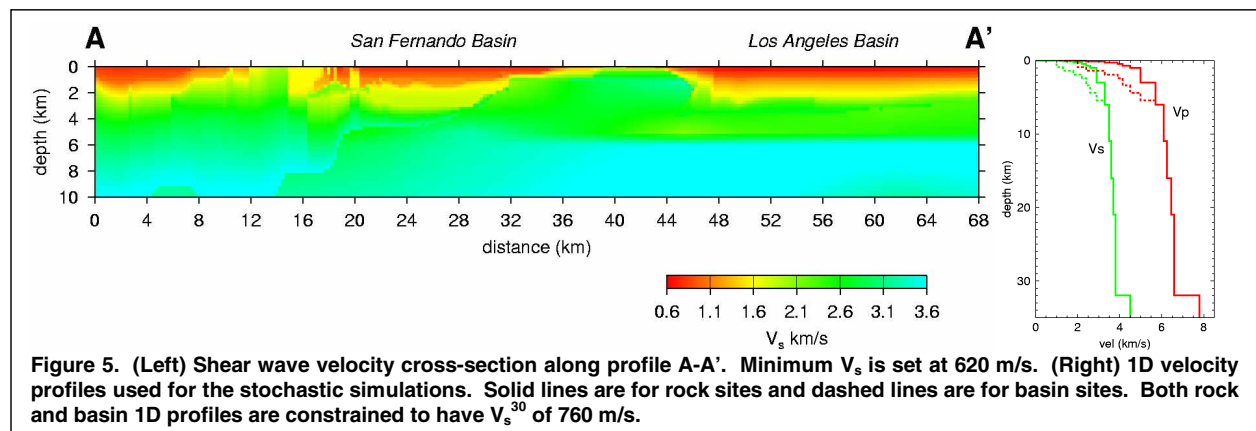
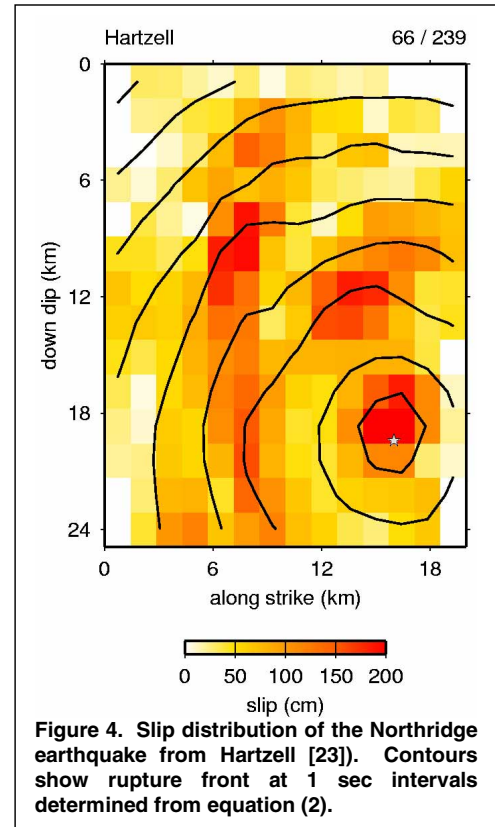
In practice, we apply these amplification functions to the amplitude spectra of the Fourier transformed simulated time histories. This process is done to the deterministic and stochastic results separately since these may have different computational reference velocities. Although the amplification factors are strictly defined for response spectra, the application in the Fourier domain appears to be justified since the functions vary slowly with frequency. Finally, the individual responses are combined into broadband response using a set of matched butterworth filters. The filters are 4<sup>th</sup>-order and zero-phase with a lowpass corner at 1 Hz for the deterministic response and a highpass corner at 1 Hz for the stochastic response. The important properties of the matched filters are 1) they do not alter the phase of the response and 2) they sum to unity for all frequencies. After applying the filters to the individual responses, they are summed together to produce a single broadband time history.



The lateral complexity in the velocity structure extends far beneath the near surface layers. Figure 5 shows a vertical cross section of the shear wave velocity structure along a profile extending from NW of the San Fernando basin into the middle of the Los Angeles basin (A-A' in Figure 4). There is a clear expression of the low velocity sediments of the San Fernando and Los Angeles basins down to several km in depth. The lateral contrast between the various rock types can have a profound effect on the propagation of seismic energy, particularly at frequencies less than about 1 Hz. For this reason, we have used this complex representation of the subsurface velocity structure in our deterministic simulations.

From the 3D velocity structure, we extract 1D velocity profiles to use in the stochastic simulations. We select one profile for rock sites and another profile for basin sites (Figure 5). Even though both 1D profiles are constrained to have  $V_s^{30}$  of 760 m/s, the basin profile has significantly lower velocities than the rock profile in the upper 5 km. This will have two primary effects on the stochastic simulations: 1) the GF travel times will more closely match the phasing of the deterministic results, which are calculated with the fully 3D model and 2) the impedance amplification determined from the quarter-wavelength approach will have a broader frequency response for the basin sites compared to the rock sites.

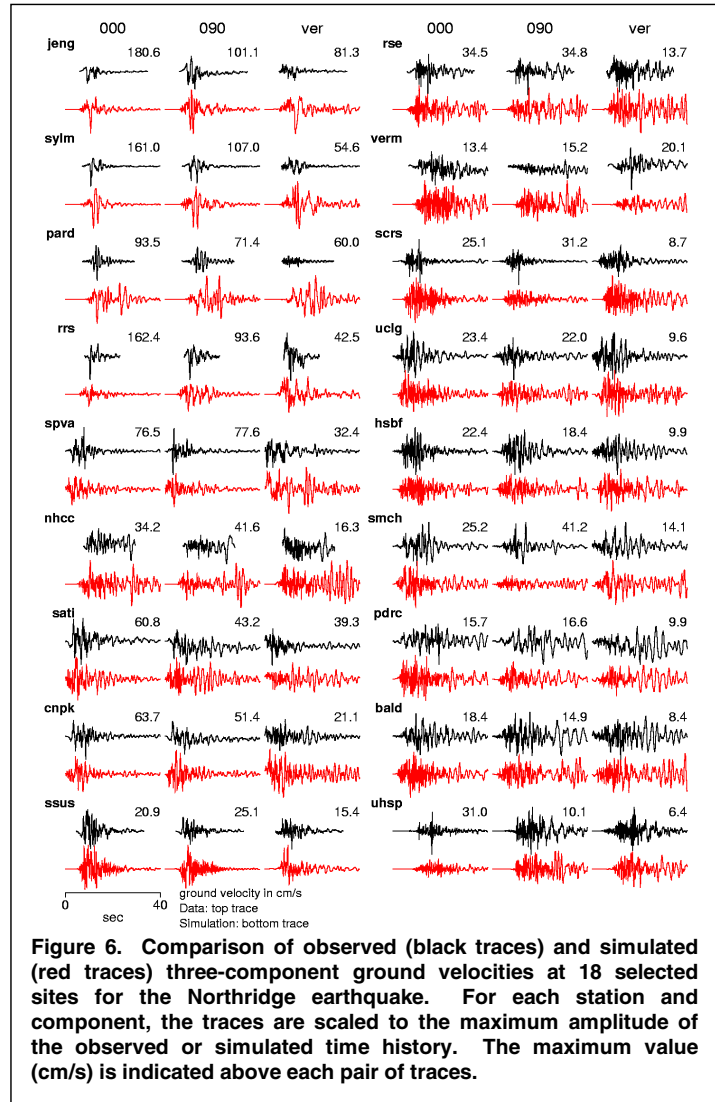
For each of the 69 strong motion sites, site category and  $V_s^{30}$  values are obtained from Wills [22]. Using equation (5), we then construct frequency-dependent amplification functions that are applied to the results of the deterministic and stochastic simulations. The final simulated broadband time histories are computed using the match-filter and summation procedure described earlier. Figure 6 compares the observed and simulated three-component ground velocities at 18 selected sites. These 18 sites include near-fault locations (e.g., rrs), rock sites (e.g., ssus) and deep basin sites (e.g. pdrc). In general, the waveform character, amplitude and duration of the observed data are matched reasonable well by the simulation. The simulation reproduces key phenomena such as the pulse-like motions at forward directivity sites (jeng, sylm, pard, rrs), the relatively brief duration and higher frequency motions at rock sites (ssus, scrs), and the relatively long duration and lower frequency motions at deep basin sites (verm,



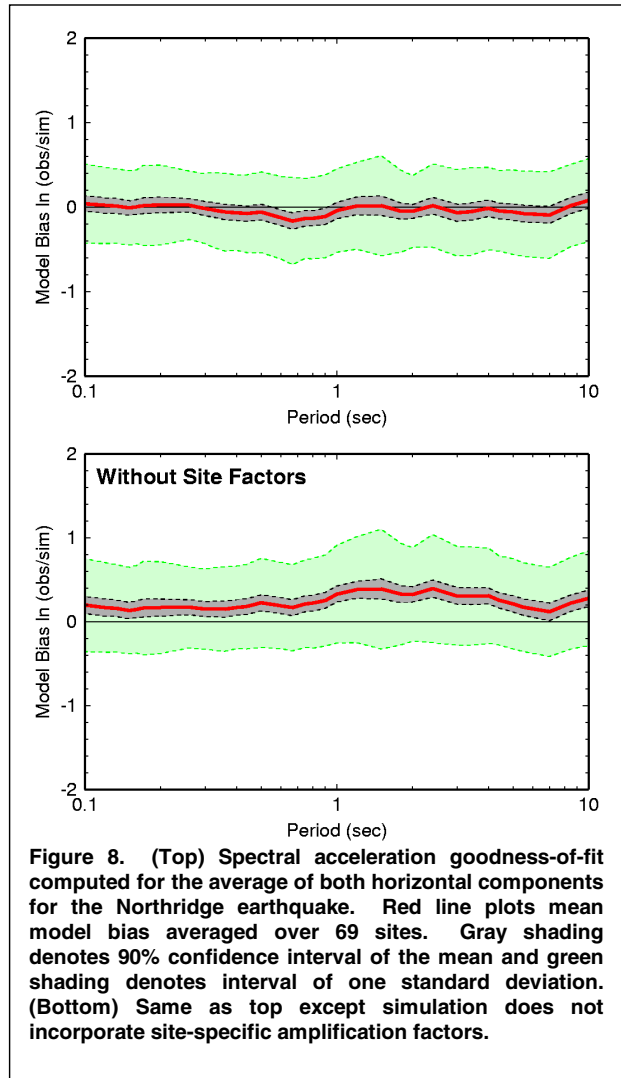
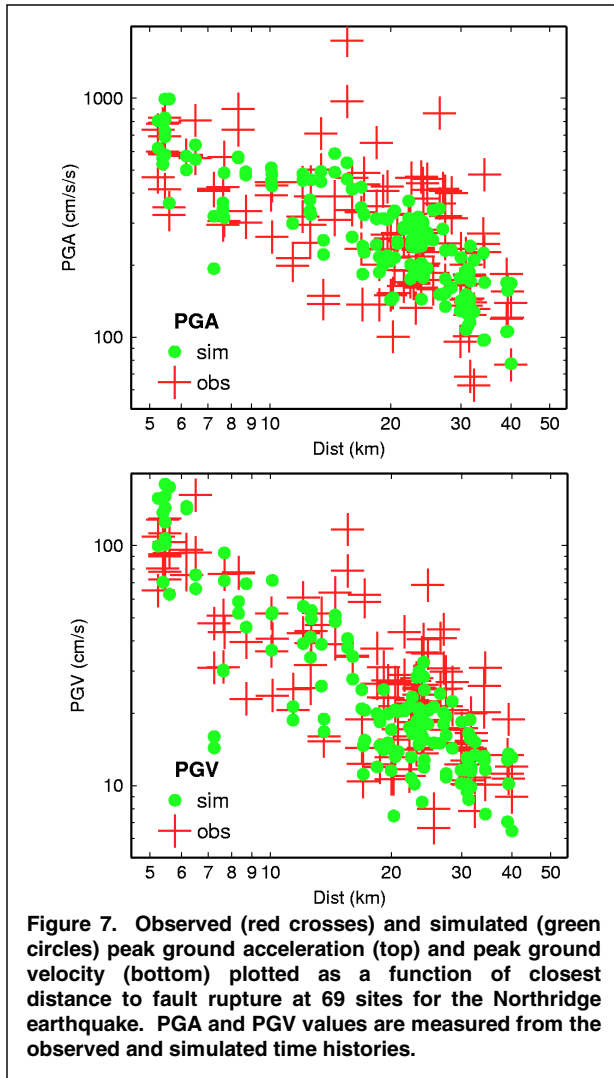
pdrc, bald). The simulation does not match exactly the phasing of the observed waveforms, as we expect since we have used a smooth representation of the rupture process. In addition, we do not predict several of the large-amplitude high-frequency pulses seen in the data (e.g., scrs, uhsp) due to the use of random phasing in the stochastic calculations.

Figure 7 compares the observed and simulated PGA and PGV for all 69 sites. These values are plotted as a function of closest distance to the rupture plane. The agreement between the observed and simulated values is good, both in terms of amplitude level and distance dependence. The simulation also reproduces several important features seen in the observations. These include: 1) the flattening of PGA attenuation between 10 km and 20 km distance, which is likely due to hanging wall effects and amplification within the San Fernando basin, 2) the large PGV at close distance, which results from strong forward directivity effects, and 3) the elevation in PGA and PGV around 25 km distance, which is probably due to amplification effects along the northern margin of the Los Angeles basin.

We also compare the data and simulations using goodness-of-fit measures for 5% damped spectral acceleration calculated from the broadband time histories (e.g., Schneider [25]). For an individual station, the residual  $r(T_i)$  at each period  $T_i$  is given by  $r(T_i) = \ln[sa_O(T_i)/sa_S(T_i)]$ , where  $sa_O(T_i)$  and  $sa_S(T_i)$  are the observed and simulated spectral acceleration values, respectively. The model bias is obtained by averaging the residuals for all stations and both horizontal components at each period. A model bias of zero indicates the simulation, on average, matches the observed ground motion level. A negative model bias indicates over-prediction and a positive model bias indicates under-prediction of the observations. The top panel of Figure 8 plots the model bias and standard error for the Northridge simulation. The simulation result has no significant bias over the period range 0.1 to 10 seconds, indicating that the simulation model adequately captures the main characteristics of the ground motion response. In addition, the standard error is about 0.4 to 0.5 (natural log) over this period band. The bottom panel plots the model bias for the simulation when the site-specific amplification factors are not included in the response. Without the site-specific amplification factors, the simulation under-predicts the observed response by about 20 to 30%, with the largest difference at the longer periods. More significantly, the standard error increases to about 0.6 to 0.7. This indicates that including the site-specific factors significantly reduces the uncertainty of the ground motion estimates.



**Figure 6. Comparison of observed (black traces) and simulated (red traces) three-component ground velocities at 18 selected sites for the Northridge earthquake. For each station and component, the traces are scaled to the maximum amplitude of the observed or simulated time history. The maximum value (cm/s) is indicated above each pair of traces.**



We also examine the spectral acceleration residuals as a function of site type and location. Figure 9 plots the residuals as a function of distance to the rupture plane at periods of 0.3, 1.0 and 3.0 sec. The sites are grouped into three categories using the classification of Wills [22], B-BC, C-CD, and D. These plots indicate that there is little systematic trend in the residuals as a function of site type or distance for these periods. Figure 10 displays the residuals in map view. These plots indicate some slight trends in the simulations such as a tendency to under-predict the response along the Santa Monica Mountains and northern Los Angeles basin, and a tendency to over predict the response in the San Fernando basin and downtown Los Angeles regions, particularly at the longer periods.

### 1989 Loma Prieta earthquake

Our model region for the Loma Prieta earthquake covers the area within about 35 km of the rupture surface, which includes 32 strong ground motion recording sites (Figure 11). Site types range from  $V_s^{30}$  categories BC to D (Wills [22]). We adopt the fault geometry of Wald [26] for our simulations. The fault is 40 km long and has a down-dip width of 20 km. The strike is  $130^\circ$ , dip is  $70^\circ$  and the rake averages about  $150^\circ$ . We use a moment of  $2.53 \times 10^{26}$  dyne  $\cdot$  cm, giving a moment magnitude of 6.9.

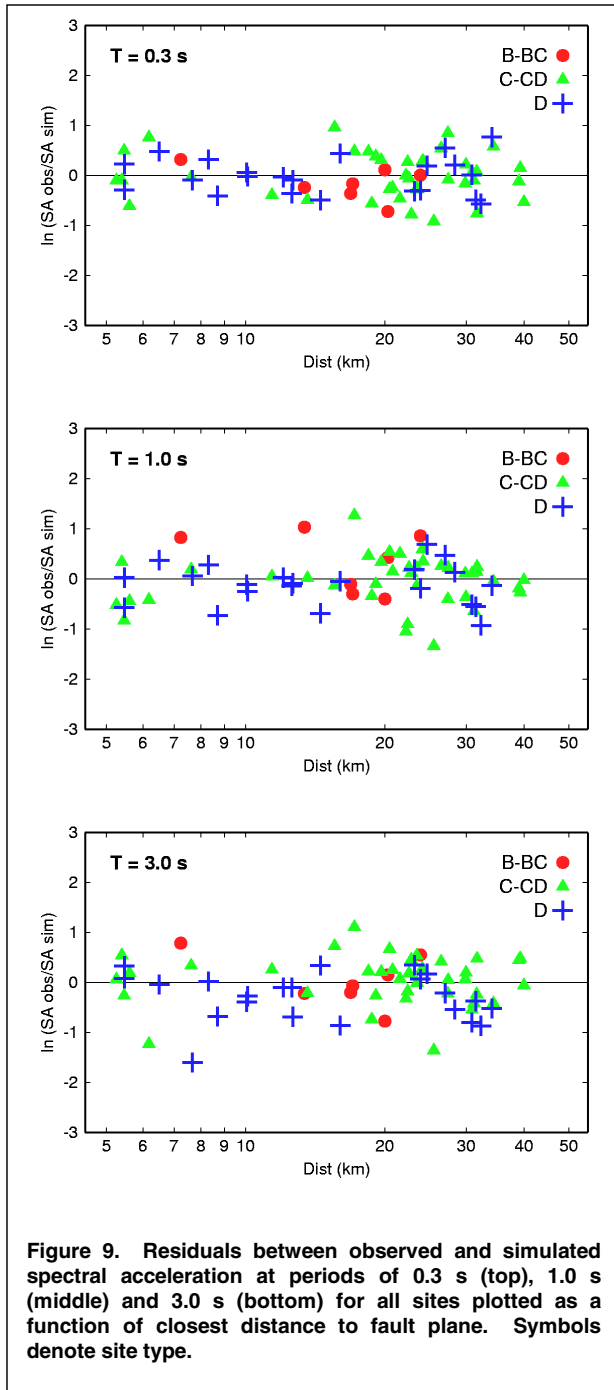


Figure 9. Residuals between observed and simulated spectral acceleration at periods of 0.3 s (top), 1.0 s (middle) and 3.0 s (bottom) for all sites plotted as a function of closest distance to fault plane. Symbols denote site type.

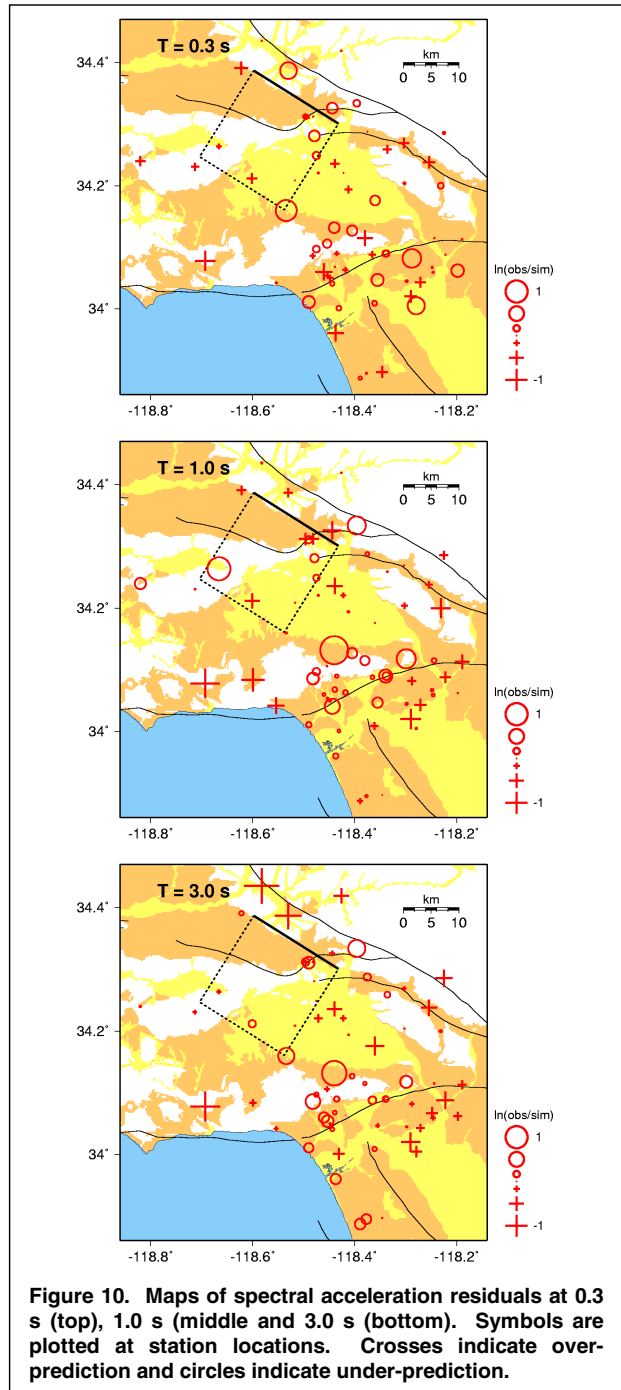


Figure 10. Maps of spectral acceleration residuals at 0.3 s (top), 1.0 s (middle) and 3.0 s (bottom). Symbols are plotted at station locations. Crosses indicate over-prediction and circles indicate under-prediction.

Figure 12 shows the final static slip distribution obtained from Wald [26]. The hypocenter is in the middle of the fault a depth of about 18 km. There are 2 main asperities; one located northwest and the other southeast of the hypocenter. The contour lines in Figure 12 indicate the propagation of the rupture front at 1 sec intervals. We have determined the rupture times using equation (2). Again, the rupture is advanced in large slip regions and is delayed in low slip regions.

The subsurface velocity structure used for the deterministic simulations is constructed using two 1D velocity profiles, one for the region west of the San Andreas fault and the other for the region east of the fault (Figure 13). Above 17 km depth, the velocities on the west side of the fault are about 5% higher than

the velocities on the east side of the fault. These profiles are taken from Stidham [27], who found that the lateral velocity contrast across the San Andreas fault had a strong influence on wave propagation effects during the Loma Prieta earthquake. In particular, energy propagating along the fault is laterally refracted toward the eastern side due to the velocity contrast. This tends to increase the amplitudes of waves traveling northward into the Santa Clara Valley and southeastward into the Gilroy and Hollister areas. We set the lowest shear wave velocity to be 1000 m/s in our simulations. With a minimum finite-difference grid spacing of 200 m in the lowest velocity regions of the model, we obtain reliable results for frequencies of about 1 Hz and less.

Several studies have proposed 3D basin velocity models for this region, including Brocher [28] and Stidham [27]. In our current simulations we have not included these more detailed structural representations, mainly because there are some notable differences between the proposed models, and we did not want the uncertainty in the 3D velocity structure to have a strong influence on the uncertainty in our ground motion estimates. We fully expect that future refinement of the 3D velocity structure will also improve the simulation results.

For the stochastic simulations, we have used the same basic 1D profiles that are used for the deterministic calculations. The only modification is that both models are tapered in the near-surface to have a  $V_s^{30}$  of 760 m/s. Again, impedance amplification effects at high frequencies are modeled using the quarter-wavelength approach.

For each of the 32 strong motion sites, site category and  $V_s^{30}$  values are obtained from Wills [22]. Using equation (5), we then construct frequency-dependent amplification functions that are applied to the results of the deterministic and stochastic simulations. The final simulated broadband time histories are computed using the match-filter and summation procedure described earlier. Figure 14 compares the observed and simulated three-component ground velocities at 18 selected sites. These 18 sites include near-fault locations (e.g., lgpc), rock sites (e.g., lex1) and Santa Clara Valley sites (e.g. sjin). In general, the waveform character, amplitude and duration of the observed data are matched reasonable well by the simulation. The simulation reproduces key phenomena such as the pulse-like motions at forward directivity sites (lgpc, lex1, srtg), the longer duration and non-pulse-like motions at neutral directivity near-fault sites (bran, cor), and the relatively long duration and lower frequency motions at the more distant sites (sjin, agnw, hall).

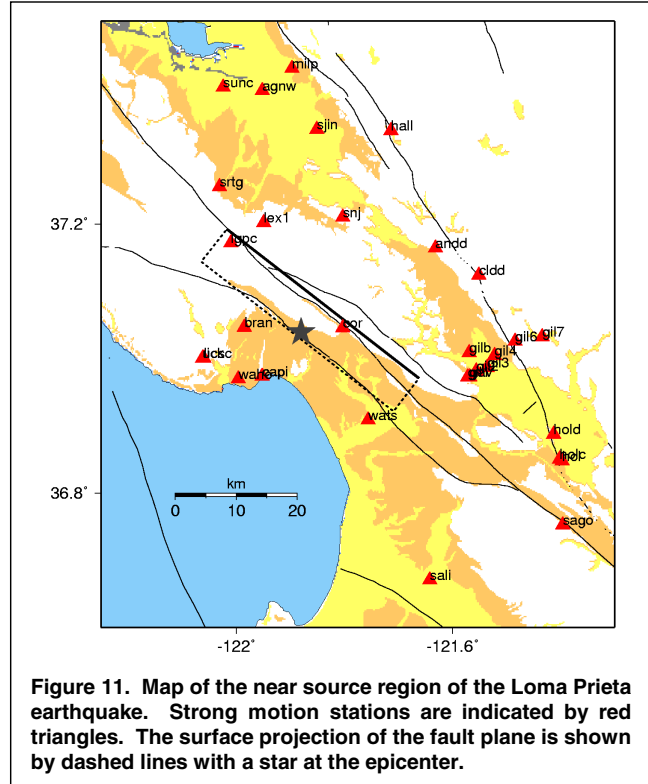


**Figure 11. Map of the near source region of the Loma Prieta earthquake. Strong motion stations are indicated by red triangles. The surface projection of the fault plane is shown by dashed lines with a star at the epicenter.**

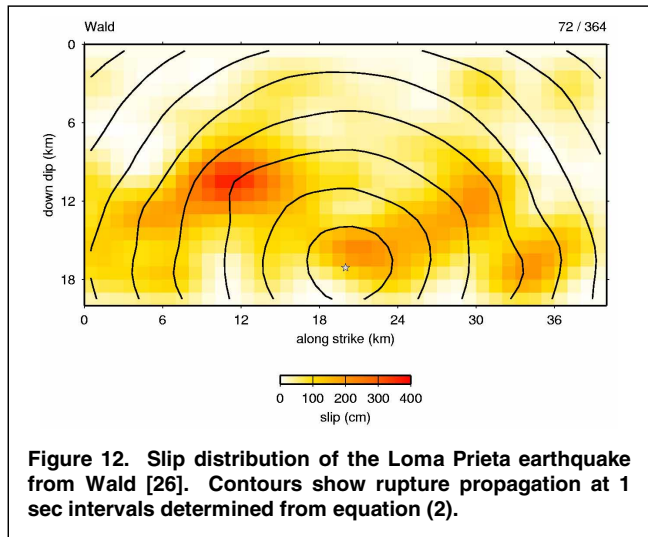
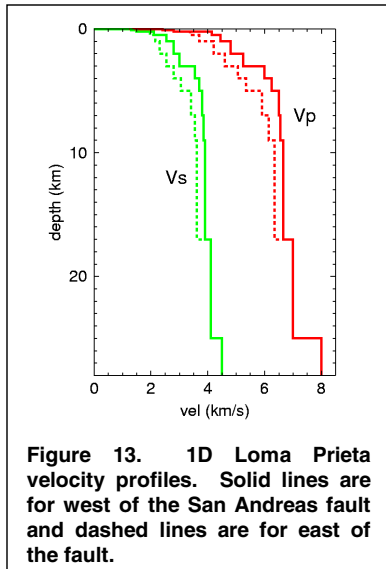


**Figure 12. Slip distribution of the Loma Prieta earthquake from Wald [26]. Contours show rupture propagation at 1 sec intervals determined from equation (2).**

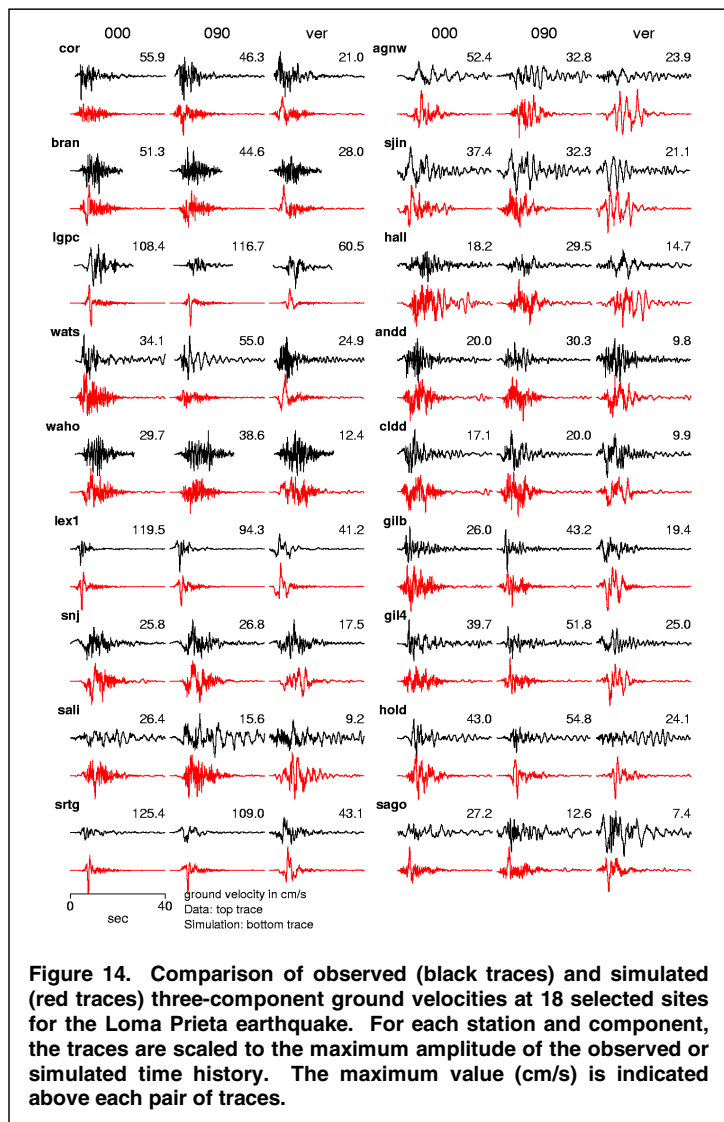


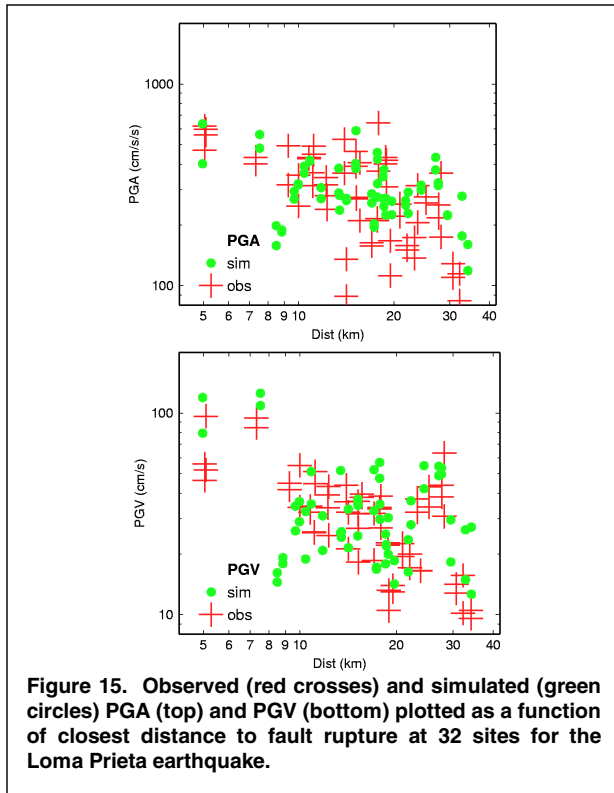
We also compare the data and simulations using the same goodness-of-fit measures for 5% damped spectral acceleration calculated from the broadband time histories that we described earlier for the Northridge simulation. Figure 16 plots the model bias and standard error for the Loma Prieta simulation. On average, the simulation result tends to slightly over-predict the recorded motions (on the order of 5 to 10%), which could be accounted for by adjusting the moment used in the simulation. Aside from this feature, there is no significant bias over the period range 0.1 to 10 seconds, indicating that the simulation model adequately captures the main characteristics of the ground motion response. In addition, the standard error is about 0.4 (natural log) over this period band.

As was done in the Northridge comparison, we also examine the spectral acceleration residuals as a function of site type and location. Figure 17 plots the residuals as a function of distance to the rupture plane at periods of 0.3, 1.0 and 3.0 sec. The sites are grouped into three categories using the classification of Wills [22], B-BC, C-CD, and D. These plots indicate that there is little systematic trend in the residuals as a function of site type or distance for these periods. Figure 18

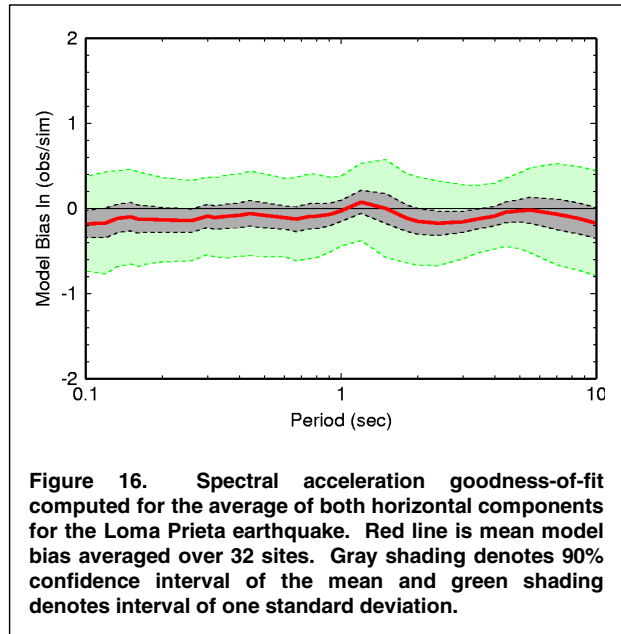
As with the Northridge simulation, we do not match exactly the phasing of the observed waveforms, which is to be expected since we use a smooth representation of the rupture process.

Figure 7 compares the observed and simulated PGA and PGV for all 32 sites. These values are plotted as a function of closest distance to the rupture plane. The agreement between the observed and simulated values is good, both in terms of amplitude level and distance dependence. The simulation also reproduces several important features seen in the observations. These include: 1) the flattening of PGA attenuation between 10 km and 20 km distance, which may be related to site response (most of these sites are soil), 2) the large PGV at close distance, which results from strong forward directivity effects, and 3) the elevation in PGA and PGV around 22 - 30 km distance, which is probably due to amplification effects in the Santa Clara Valley and the Gilroy / Hollister area.





**Figure 15. Observed (red crosses) and simulated (green circles) PGA (top) and PGV (bottom) plotted as a function of closest distance to fault rupture at 32 sites for the Loma Prieta earthquake.**



**Figure 16. Spectral acceleration goodness-of-fit computed for the average of both horizontal components for the Loma Prieta earthquake. Red line is mean model bias averaged over 32 sites. Gray shading denotes 90% confidence interval of the mean and green shading denotes interval of one standard deviation.**

displays the residuals in map view. These plots suggest some systematic behavior of the residuals, such as over-prediction in the Santa Clara Valley and under-prediction in Gilroy at 0.3 sec period; under-prediction in the near-fault region at 1 second period, and under-prediction in the Santa Clara Valley at 3 sec period. However, in general, these trends are of relatively small magnitude, and we suspect that increased knowledge of the 3D sub-surface geology will improve the simulation response.

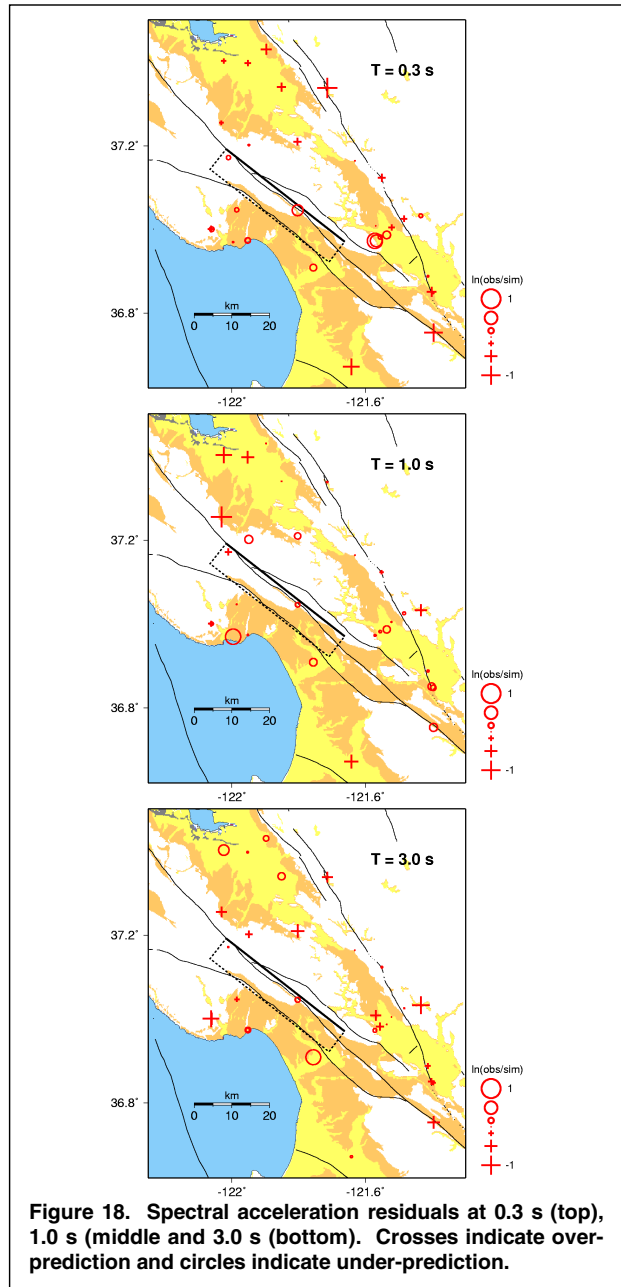
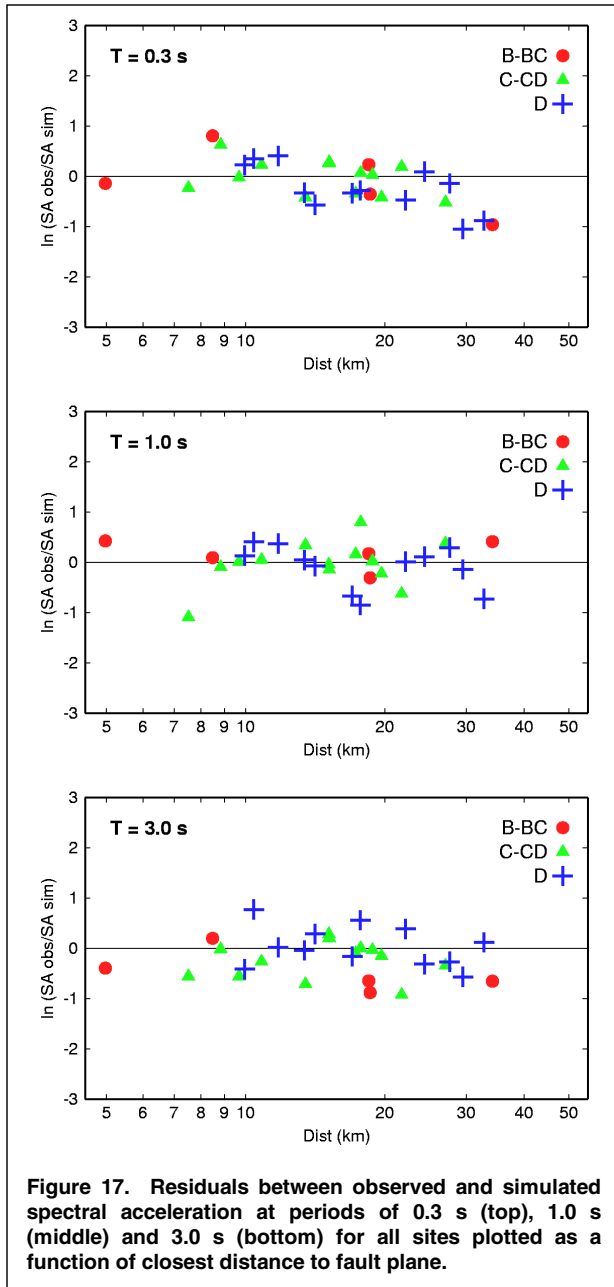
## DISCUSSION AND CONCLUSIONS

The broadband simulation methodology presented here provides a general framework for synthesizing ground motion time histories for future scenario earthquakes. One of the main enhancements of our approach over previous techniques is the use of frequency-dependent non-linear site amplification factors. Our methodology produces quite favorable results when compared against the strong ground motions recorded during the 1989 Loma Prieta and 1994 Northridge earthquakes.

In developing this methodology, we have tried to incorporate as much detail as possible in describing the source, path and site effects in order to adequately capture the main characteristics of the expected ground motions. For the path and site effects, this stresses the importance of developing detailed 3D seismic velocity models for earthquake prone regions. However, we recognize that extremely detailed descriptions of the earthquake rupture process will generally not be available *a priori* for future events. Thus, our methodology uses simple, yet flexible, rules to parameterize the slip, slip velocity function and rupture velocity. Our hope is that more robust constraints on these parameters can be obtained from detailed source inversion studies and dynamic rupture analyses.

## REFERENCES

1. Borchardt R. "Estimates of site-dependent response spectra for design (methodology and justification)." *Earthquake Spectra* 1994; 10(4): 617-653.
2. Hartzell S. "Earthquake aftershocks as Green's functions." *Geophys. Res. Lett.* 1978; 5: 1-4.



3. Irikura K. "Semi-empirical estimation of strong ground motions during large earthquakes." Bull. Disast. Prev. Res. Inst., Kyoto Univ. 1978; 33: 63-104.
4. Boore D. "Stochastic simulation of high frequency ground motions based on seismological models of the radiated spectra." Bull. Seism. Soc. Am. 1983; 73: 1865-1894.
5. Zeng Y, Anderson JG, Yu G. "A composite source model for computing synthetic strong ground motions." Geophys. Res. Lett. 1994; 21: 725-728.
6. Hartzell S. "Comparison of seismic waveform inversion results for the rupture history of a finite fault: application to the 1986 North Palm Springs, California, earthquake." J. Geophys. Res. 1989; 94: 7515-7534.
7. Hartzell S, Harmsen S, Frankel A, Larsen S. "Calculation of broadband time histories of ground motion: comparison of methods and validation using strong ground motion from the 1994 Northridge earthquake." Bull. Seism. Soc. Am. 1999; 89: 1484-1504.

8. Hartzell S, Heaton T. "Inversion of strong ground motion and teleseismic waveform data for the fault rupture history of the 1979 Imperial Valley, California earthquake." *Bull. Seism. Soc. Am.* 1983; 73: 1553-1583.
9. Graves R. "Simulating seismic wave propagation in 3D elastic media using staggered grid finite differences." *Bull. Seism. Soc. Am.* 1996; 86: 1091-1106.
10. Pitarka A. "3D elastic finite difference modeling of seismic wave propagation using staggered grid with non-uniform spacing." *Bull. Seism. Soc. Am.* 1998; 88: 54-68.
11. Day S, Bradley C. "Memory efficient simulation of anelastic wave propagation." *Bull. Seism. Soc. Am.* 2001; 91: 520-531.
12. Guatteri M, Mai PM, Beroza G, Boatwright J. "Strong ground motion prediction from stochastic-dynamic source models." *Bull. Seism. Soc. Am.* 2003; 93: 301-313.
13. Somerville P, Irikura K, Graves R, Sawada S, Wald D, Abrahamson N, Iwasaki Y, Kagawa T, Smith N, Kowada A. "Characterizing crustal earthquake slip models for the prediction of strong ground motion." *Seism. Res. Lett.* 1999; 70: 59-80.
14. Kagawa T, Irikura K, Somerville P. "A study on ground motion and fault rupture due to subsurface faults." *Eos. Trans. AGU* 2001; 82(47): Fall Meet. Suppl., Abstract S31C-06.
15. Hisada Y. "A theoretical omega-square model considering spatial variation in slip and rupture velocity. part 2. case for a two-dimensional source model." *Bull. Seism. Soc. Am.* 2001; 91: 651-666.
16. Mai P, Beroza G. "A spatial random field model to characterize complexity in earthquake slip." *J. Geophys. Res.* 2002; 107(B11): doi:10.1029/2001JB000588.
17. Beresnev I, Atkinson G. "Modeling finite fault radiation from the  $\omega^n$  spectrum." *Bull. Seism. Soc. Am.* 1997; 87: 67-84.
18. Beresnev I, Atkinson G. "Subevent structure of large earthquakes - A ground motion perspective." *Geophys. Res. Lett.* 2001; 28(1): 53-56.
19. Beresnev I, Atkinson G. "Stochastic finite fault modeling of ground motions from the 1994 Northridge, California earthquake. I. validation on rock sites." *Bull. Seism. Soc. Am.* 1998; 88: 1392-1401.
20. Ou GB, Herrmann R. "A statistical model for ground motion produced by earthquakes at local and regional distances." *Bull. Seism. Soc. Am.* 1990; 80: 1397-1417.
21. Boore D, Joyner W, "Site amplification for generic rock sites." *Bull. Seism. Soc. Am.* 1997; 87: 327-341.
22. Wills C, Petersen M, Bryant W, Reichle M, Saucedo G, Tan S, Taylor G, Treiman J. "A site conditions map for California based on geology and shear wave velocity." *Bull. Seism. Soc. Am.* 2000; 90(6B): S187-S208.
23. Hartzell S, Liu P, Mendoza C. "The 1994 Northridge, California earthquake: Investigation of rupture velocity, risetime, and high frequency radiation." *J. Geophys. Res.* 1996; 101; 20,091-20,108.
24. Magistrale H, Day S, Clayton R, Graves R. "The SCEC Southern California reference three-dimensional seismic velocity model version 2." *Bull. Seism. Soc. Am.* 2000; 90(6B): S77-S94.
25. Schneider J, Silva W, Stark C. "Ground motion model for the 1989 M6.9 Loma Prieta earthquake including effects of source, path and site." *Earthquake Spectra* 1993; 9: 251-287.
26. Wald D, Helmberger D, Heaton T. "Rupture history of the 1989 Loma Prieta, California earthquake." *Bull. Seism. Soc. Am.* 1991; 81: 1540-1572.
27. Stidham C, Antolik M, Dreger D, Larsen S, Romanowicz B. "Three-dimensional structure influences on the strong motion wavefield of the 1989 Loma Prieta earthquake" *Bull. Seism. Soc. Am.* 1999; 99: 1184-1202.
28. Brocher T, Brabb R, Catchings R, Fuis G, Fumal T, Jachens R, Jayko A, Kayen R, McLaughlin R, Parsons T, Rymer M, Stanley R, Wentworth C. "A crustal-scale 3D seismic velocity model for the San Francisco Bay area, California." *Eos* 1997; 78; F435-F436.